Supplementary Information

Understanding plasma-ethanol non-equilibrium electrochemistry during the synthesis of metal oxide quantum dots

Dilli babu Padmanaban, [a*] Ruairi McGlynn, [a] Emily Byrne, [b] Tamilselvan Velusamy, [a] Małgorzata Swadźba-Kwaśny, [b] Paul Maguire [a] and Davide Mariotti [a].

[a] *Nanotechnology & Integrated Bio-Engineering Centre, Engineering Research Institute, Ulster University-Jordanstown, Belfast, UK.*

[b] *QUILL Research Centre, School of Chemistry and Chemical Engineering, Queen's University Belfast. UK.*

**E-mail: db.padmanaban@ulster.ac.uk, pdillib@gmail.com.*

Table S1. Comparison of different CuO synthesis methods with precursors and conditions.

Ref.	Synthesis method	Mean diameter (range)	Precursors	Surfactant	Comments
1	Laser Ablation Synthesis & annealing	11 nm (6-17 nm)	Copper solid, water and air	Not used	• Long annealing (10 h) required post-ablation • Broad size distribution • Size > 10 nm
2	Activated Reactive Evaporation Technique	6 nm (5 –9 nm)	Copper solid, oxygen gas	Not used	• Not pure CuO phase • Minor CuO phase observed with Cu_2O phase depends on O_2 gas flow
3	Hydrothermal Synthesis	–	Copper sulphate, ammonia, sodium hydroxide	Alanine, L-phenylalanine, L-valine, L-tyrosine, citric acid, L-tartaric acid	• Size and size distribution not reported • Product filtered and washed in distilled water then dried in air
4	Sonochemical Synthesis	6 nm and L=20 W=2 nm	Copper acetate, water and dimethylformamide	Not used	• Several chemicals used leading to by-products • Product washed with doubly distilled water and dried in vacuum
5	Microwave-assisted hydrothermal process	< 1 µm	Copper acetate, cupric nitrate, urea	Not used	• Broad size distribution • Size > 10 nm • Products were washed with doubly distilled water to remove remaining Cu^{2+},NH^{4+} and dried in oven
6	Simple solution method	2-3 µm	Copper nitrate, sodium hydroxide	Hexamethylenetetramine	• Several chemicals used leading to by-products • Broad size distribution • Size > 10 nm • Samples were washed with methanol and dried in

					room-temperature
7	Colloid-thermal synthesis process	3-5 nm	Copper acetate, dimethylformamide	Not used	• Several chemicals used leading to by-products
8	Spinning disk reactor	20-30 nm	Copper sulphate, sodium carbonate	Not used	• Several chemicals used leading to by-products • Broad size distribution • Size > 10 nm • High temperature annealing required
9	Reverse micelle method	15 nm (5–25 nm)	Copper chloride, Ammonia, cyclohexane	TritonX-100, n-hexanol, n-pentanol	• Several chemicals used leading to by-products • Broad size distribution • Size > 10 nm • High temperature annealing required
10	Electrochemical synthesis	4-6 nm	Copper solid, acetonitrile and tetrahydrofuran	Tetraoctylammonium bromide	• Several chemicals used leading to by-products

Most of the techniques reported above struggle to achieve pure CuO phase nanoparticles (NPs) with diameter below 10 nm without surfactants. Several methods produce NPs with larger diameters or not quantum confined[1,3,5,6,8,9], while others produce mixed Cu-oxide phases[2]. When the size and phase purity can be achieved either high-temperature[8,9], post-synthesis purification or use of chemicals leading to by-products have been used[3-10]. Overall, our method retain advantages due to the phase purity, small size/size distribution while using raw precursor with no added chemicals. Our chemical analysis in the main manuscript reveals no by-products and the use of non-toxic chemicals with limited or no environmental impact. This support the possibility of our proposed method to be a *greener* compared to current state of the art.

1. Additional details on the process and methods

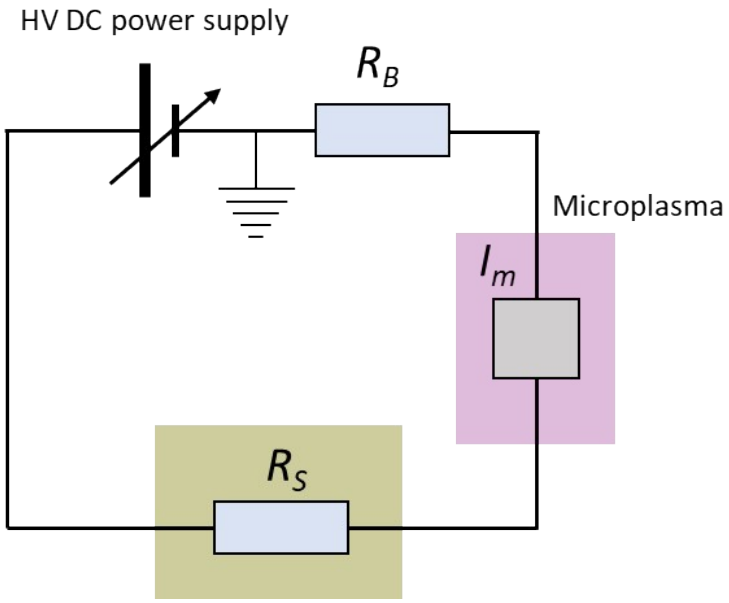

Fig. S1. Equivalent electrical circuit of plasma-liquid electrochemical cell, R_B – Ballast resistance, R_S – solution resistance, and I_m is impedance of the microplasma.

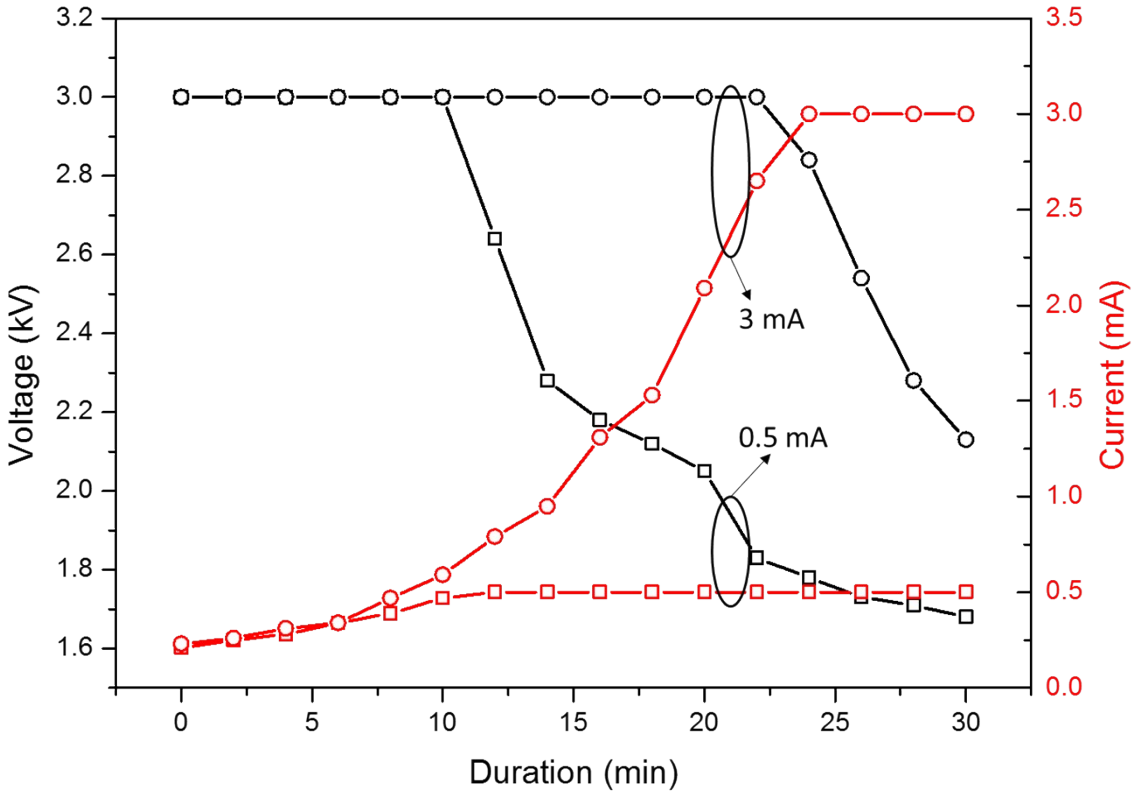

Fig. S2. Current and voltage evolution during the plasma-liquid process for Cu foil as anode for 0.5 mA and 3 mA processing currents.

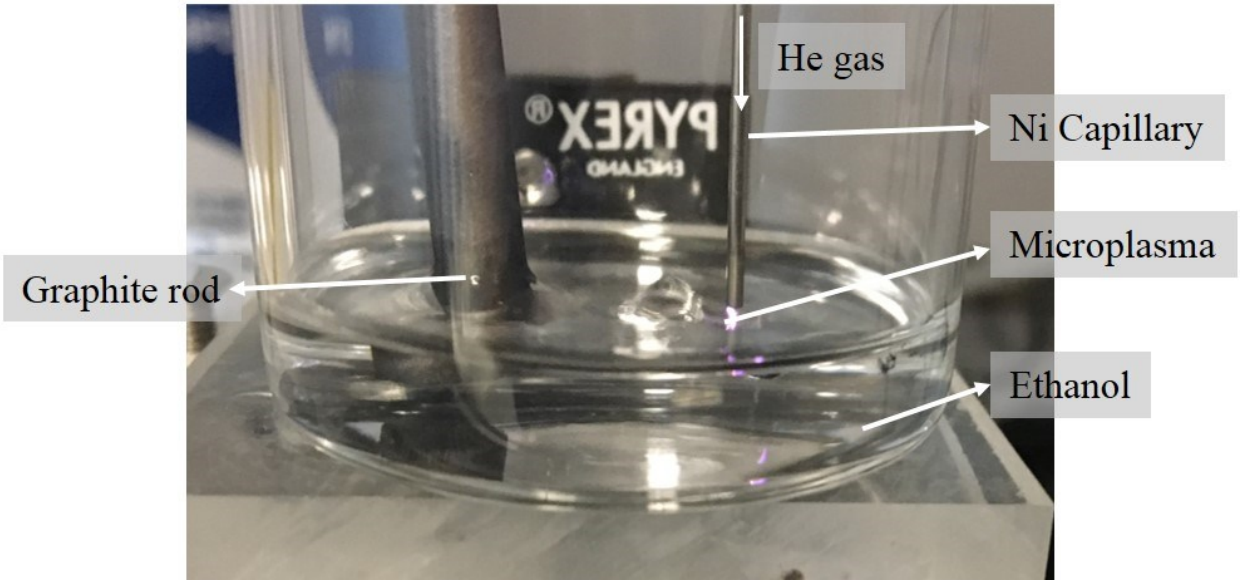

Fig. S3. Setup of plasma-liquid electrochemical cell with graphite as anode.

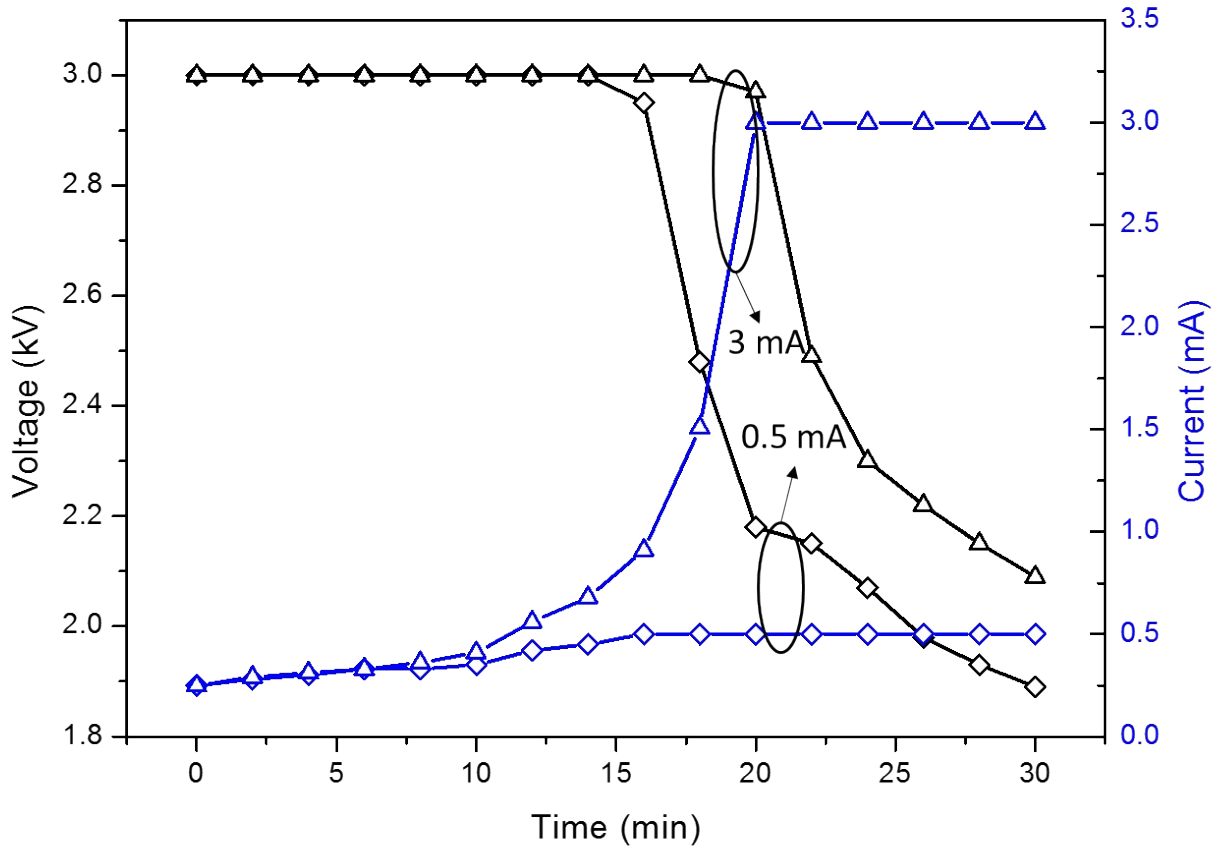

Fig. S4. Current and voltage evolution during the plasma-liquid process for graphite as anode for 0.5 mA and 3 mA processing currents.

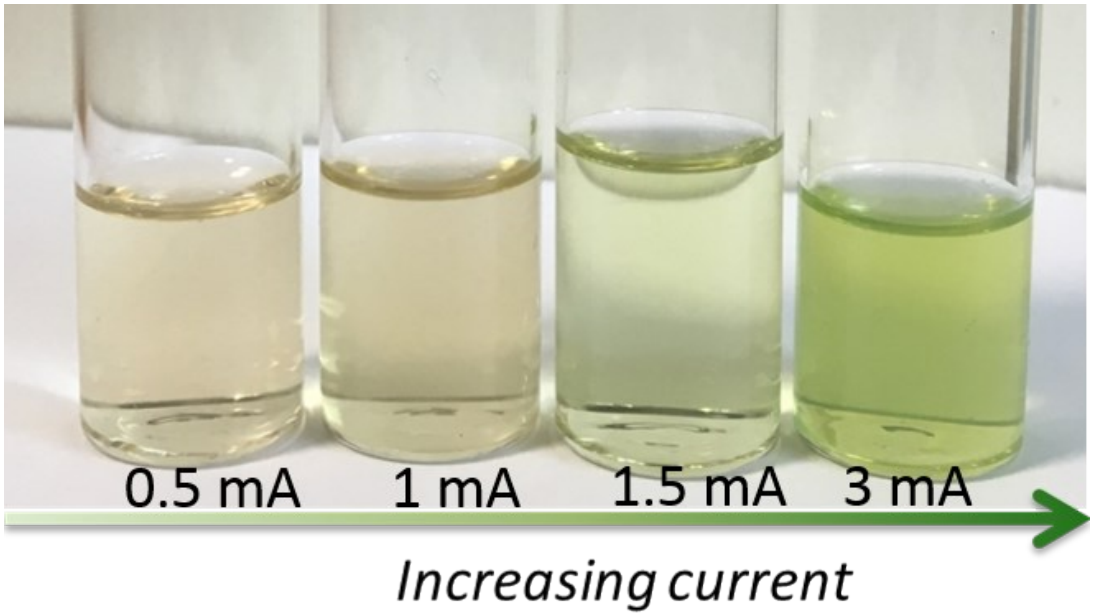

Fig. S5. Final solution obtained after plasma process for different anodic currents with Cu foil.

2. Transmission electron microscopy

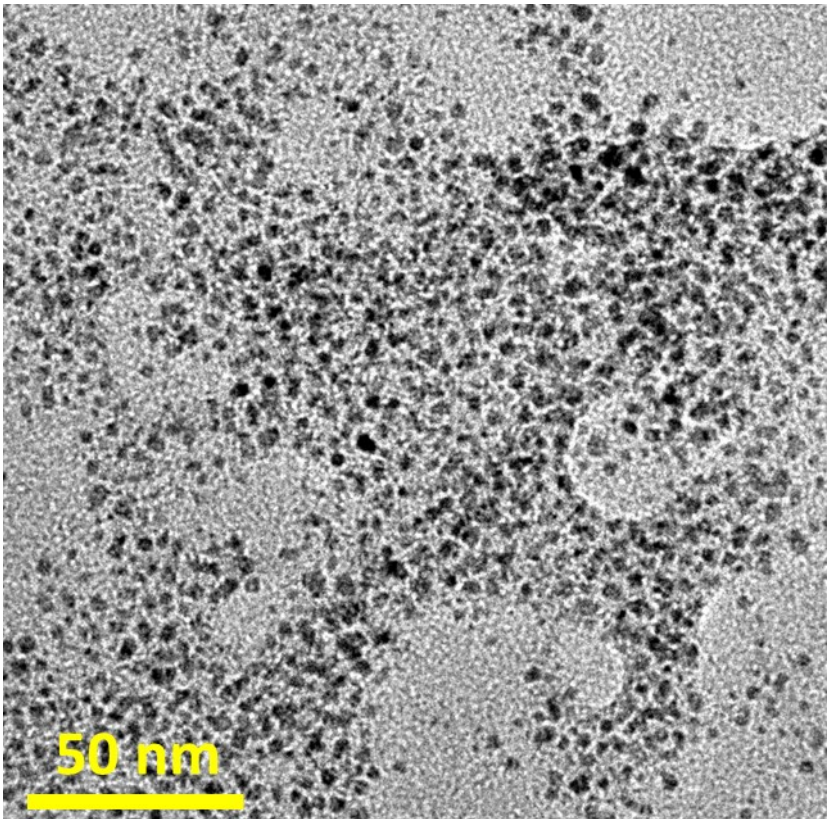

Fig. S6. Transmission electron micrographs of well dispersed CuO QDs synthesized at 0.5 mA with insets of SAED and particle size distribution.

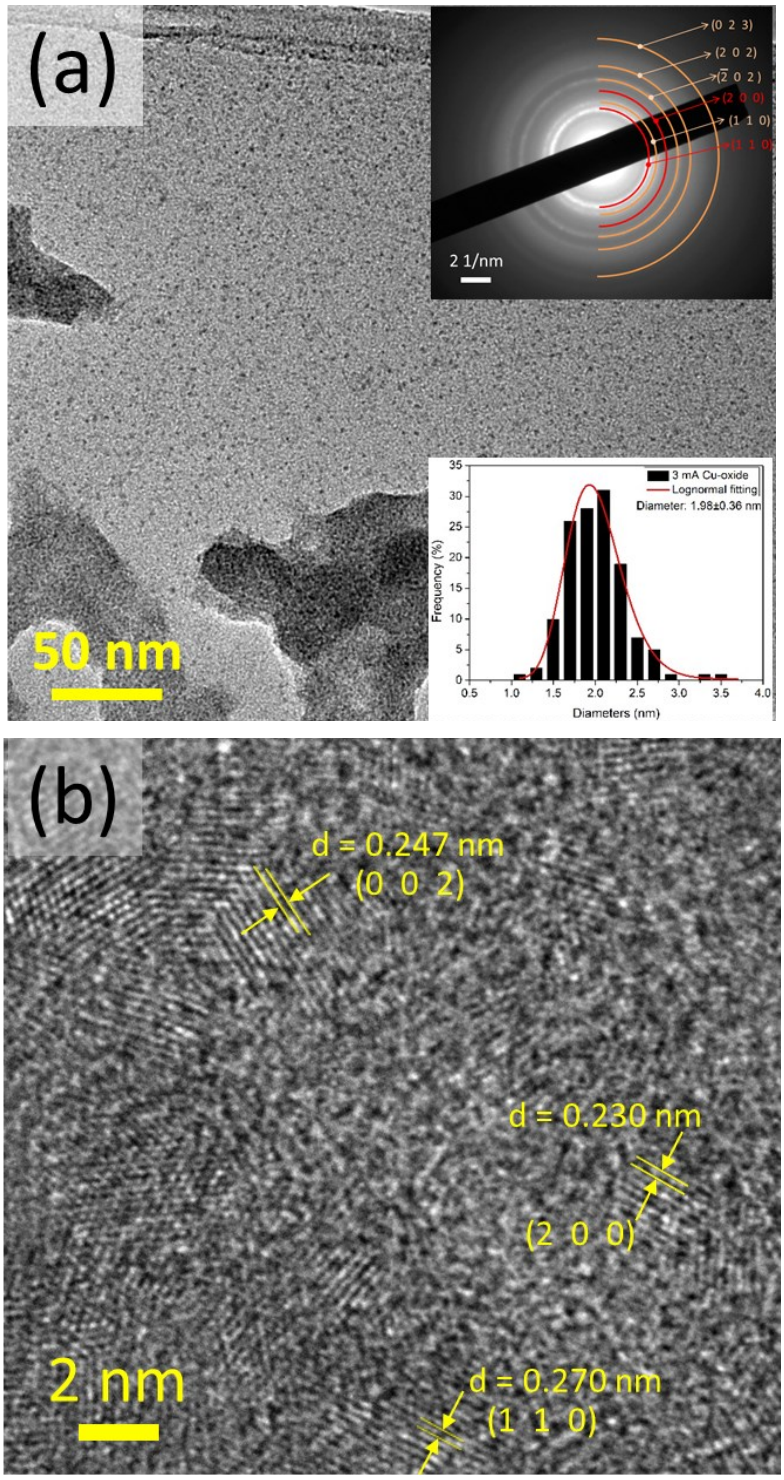

Fig. S7. Structure of CuO QDs synthesized at 3 mA: (a) transmission electron micrographs with SAED and particle size distribution (insets) and, (b) high resolution image.

3. Fourier Transform Infrared Spectroscopy

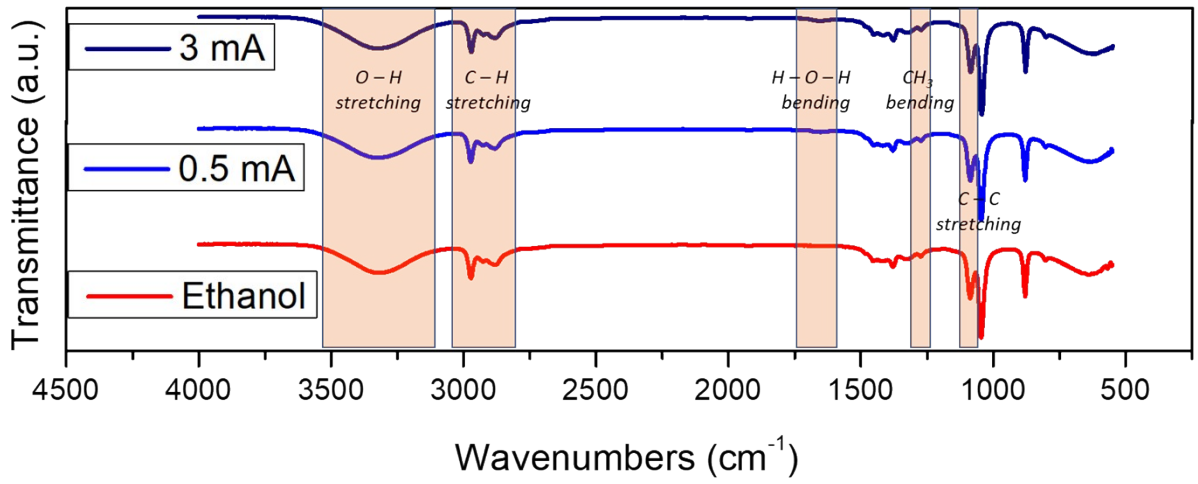

Fig. S8. Infrared transmittance from plasma processed ethanol with Cu anode comparison with two different plasma currents and untreated ethanol.

4. Nuclear Magnetic Resonance (NMR) spectroscopy

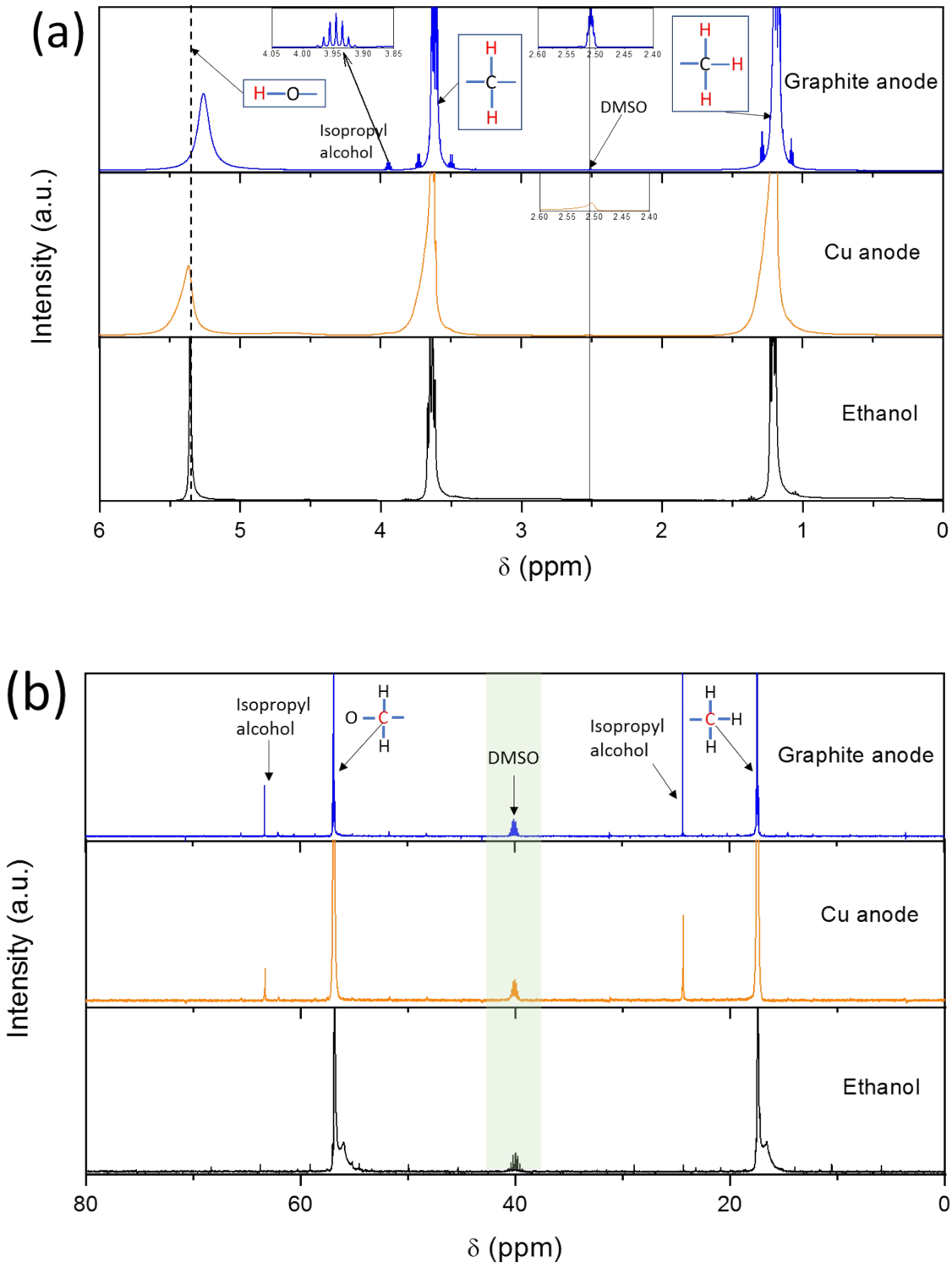

Fig. S9. NMR studies of plasma processed ethanol at 3 mA current treated for 30 minutes (a) ^{1}H NMR and (b) ^{13}C NMR spectra. Each Fig. reports the spectra for pure ethanol, plasma treatment with copper foil and graphite anodes.

5. Gas Chromatography and Mass Spectroscopy (GC-MS)

Table S2. Approximate ratio of ethanol to isopropanol present after the plasma process.

Type of anode	Current (mA)	Ethanol /IPA
Cu foil	0.5	-
	3	7 : 1
Graphite rod	0.5	38 : 1
	3	8 : 1

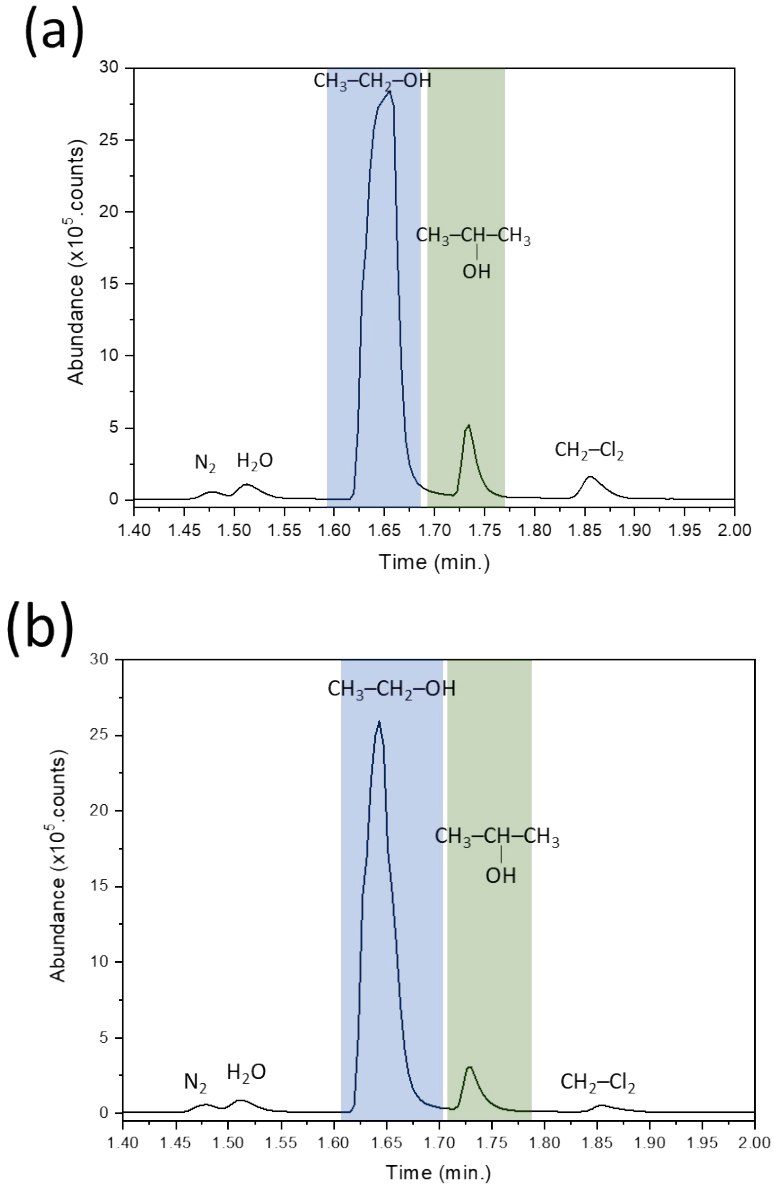

Fig. S10. Chromatogram of plasma processed ethanol at 3 mA, (a) Cu foil, and (b) graphite as anodes.

6. X-ray photoelectron spectroscopy, evolution over time

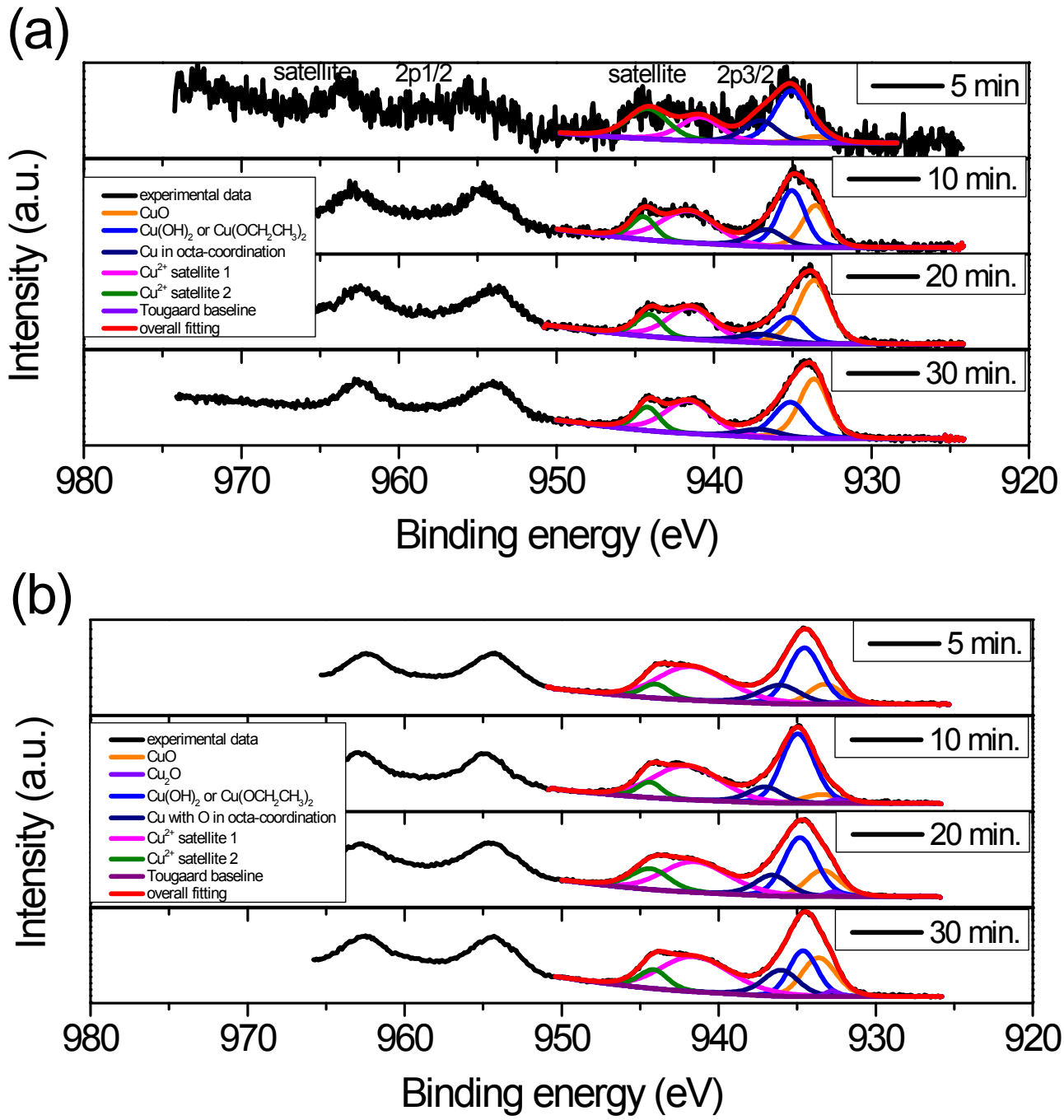

Fig. S11. *Cu 2p* core-level spectral analysis for different process intervals and two different currents (a) 0.5 mA and (b) 3 mA.

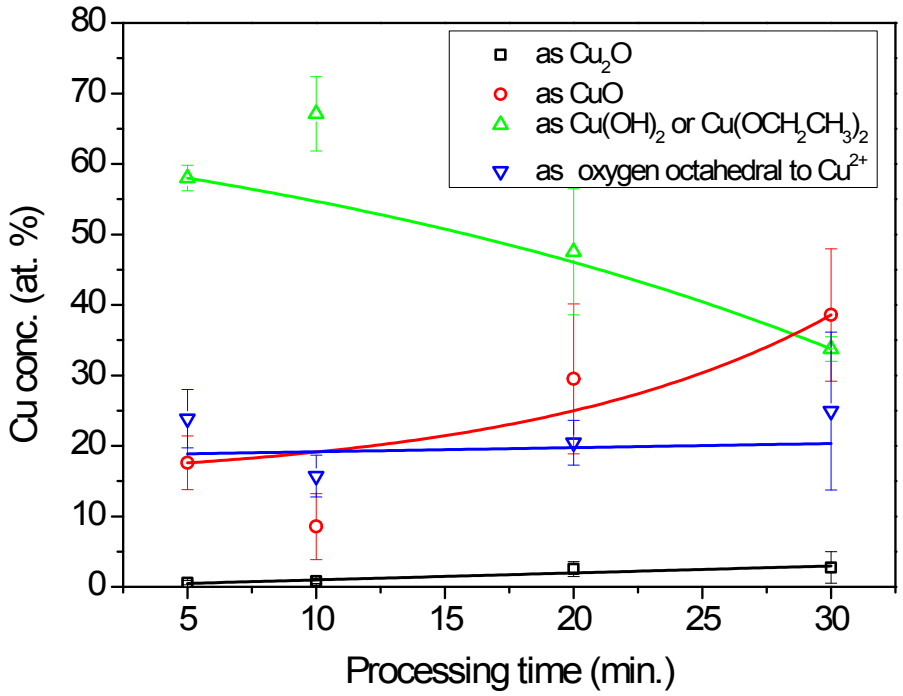

Fig. S12. Quantification of Cu/Cu^{2+} for 3 mA processed samples identifying mainly oxide and its monomer form where error bars estimated from data obtained at 3 spots.

7. Anodic dissolution and copper ion concentration measurements

Cu ion dissolution in the liquid was estimated using semiquantitative analysis through standard Cu ion test strips (QUANTOFIX 'Copper' box of 100 test sticks, 6x95 mm, Camlab - limited). Fig. S11a shows the rapid Cu ion dissolution as instantaneous change in colour of the test strip during plasma process.

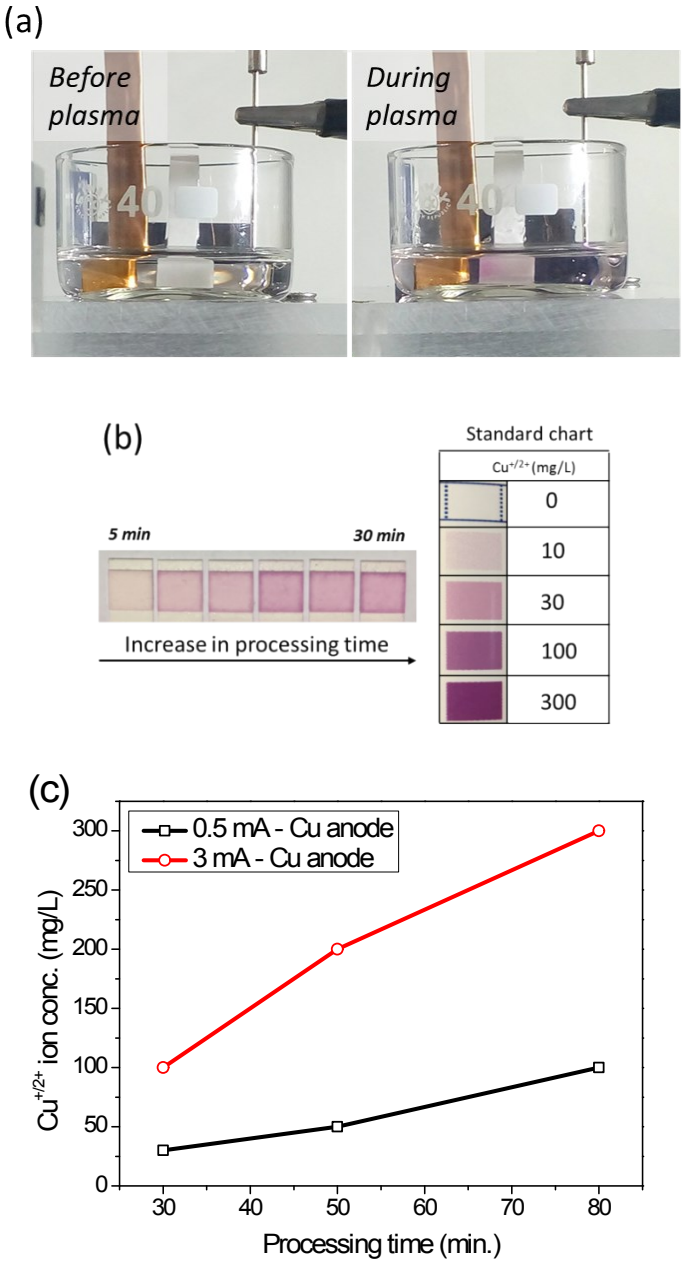

Fig. S13. (a) Rapid evolution of Cu ion less than 1 minute during plasma process, Cu ion dissolution dependence on (b) time up to 30 minutes for 0.5 mA and finally (c) Estimation of Cu ion concentration for longer duration up to total of 80 minutes for two different processing currents.

Table S3. Cu ion concentration measured with processing time for processing current - 0.5 mA, Cu anode.

Processing time (min)	**$Cu^{+/2+}$ ion concentration (mg/L)**
5	~10
10	~10 – 30
15	~10 – 30
20	~30
25	~>30
30	~>30

8. UV-Vis spectroscopy and bandgap estimation

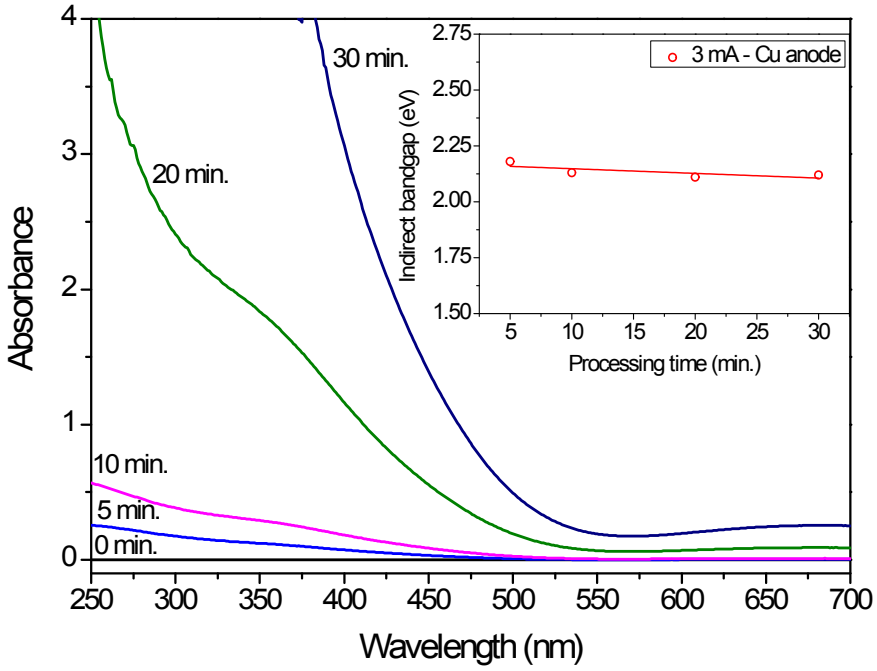

Fig. S14. (a) Absorption spectra and estimated bandgap of plasma processed ethanol at 3 mA with Cu foil.

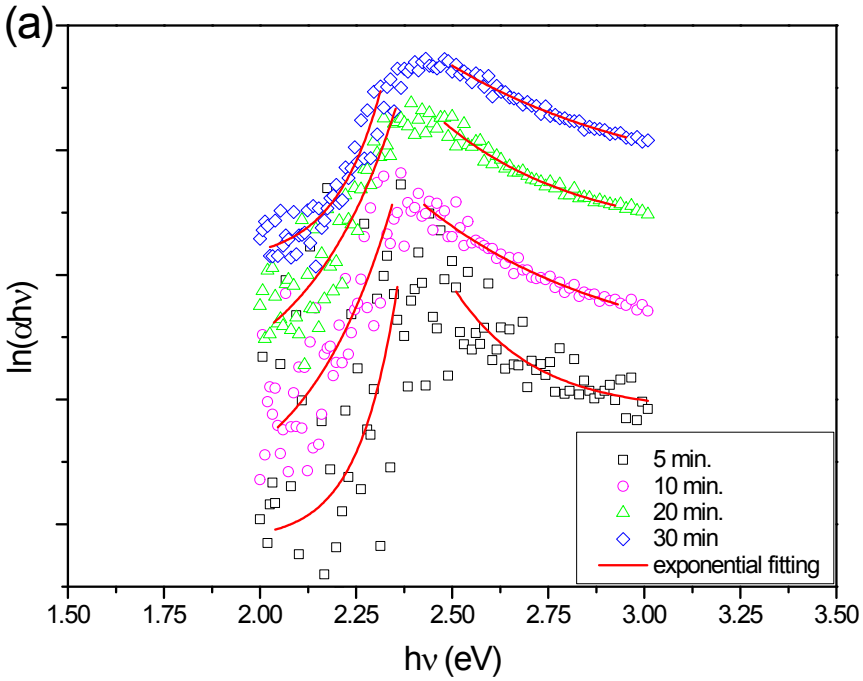

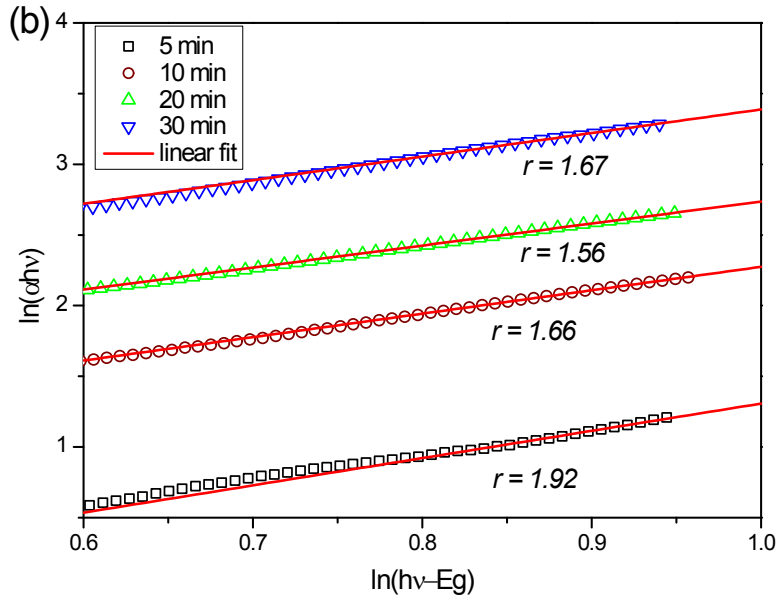

Fig. S15. (a) True nature of bandgap and (b) optical transition for 0.5 mA colloid samples.

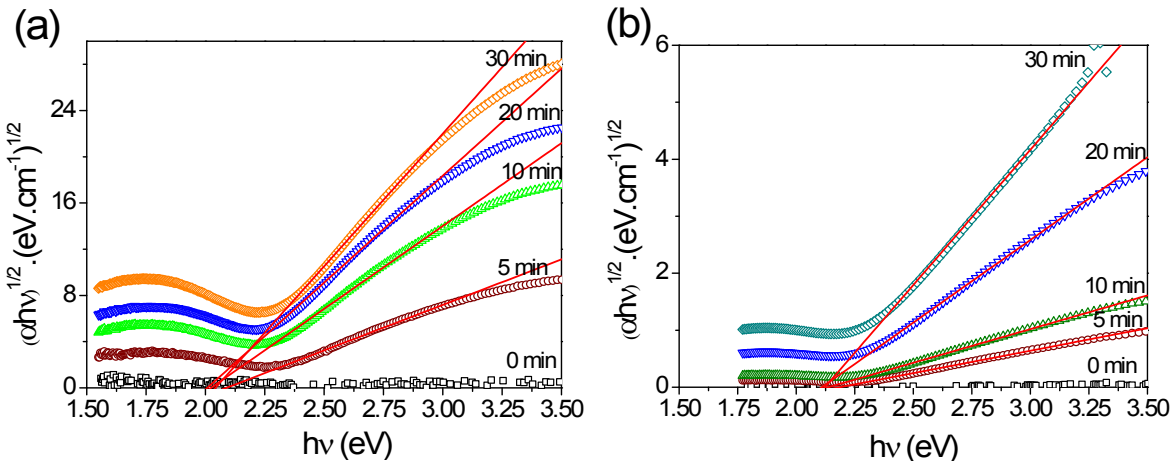

Fig. S16. Tauc's plot of obtained from absorbance spectra of plasma processed ethanol (a) 0.5 mA and (b) 3 mA currents.

For comparison, bandgap and the nature of transition '*r*' were similarly estimated as follows. Absorption coefficient (α) and absorbance (A) are related by the following relation,

$$\alpha = \frac{2.303 \times A}{t} \tag{1}$$

The absorption coefficient (α) can be written as a function of photon energy ($h\nu$) as follows,

$$\alpha h\nu = C(h\nu - Eg)^r \tag{2}$$

Where C is a constant of proportionality, E_g and r are bandgap and the nature of optical transition of the CuO QDs in the colloid respectively. The values of transition can take either any of *½, 2, 3/2*, and *3* which are related to allowed direct, allowed indirect and forbidden direct and indirect

transitions respectively.[11] To calculate the bandgap E_g without using Tauc's plot, equation 2 can be rewritten as,

$$\frac{d\ln(\alpha h\nu)}{d(h\nu)} = \frac{r}{(h\nu - Eg)} \tag{3}$$

$$\ln(\alpha h\nu) = \ln(A) + r\ln(h\nu - E_g) \tag{4}$$

Using and plotting equation (4), the value of *'r'* is estimated to be in the range 1.6-2 as shown S13b, which is suggestive of an allowed indirect transition. The nature of the transition can then be used to evaluate the bandgap with equation (3), which yields a value of ~2.39 eV at the discontinuity (Fig. S13a). The bandgap obtained using this calculation (2.39 eV) is close but higher than the one (2.1 eV) found using Tauc's plot, however in both cases this does not change over time indicating that the growth is fast and limited to the residence time of the CuO QDs within a small liquid volume below the plasma-ethanol interface. This findings are also in line with the conclusions from XPS analysis on the formation of CuO over time.

9. Hydrogen peroxide quantification

H_2O_2 concentrations was quantified here by a colorimetric technique that relies on a scavenger, titanium oxy sulphate (TOS).[12] TOS reacts with hydrogen peroxide according to the following reaction,

$$Ti^{4+} + H_2O_2 + 2H_2O \rightarrow H_2TiO_4 + 4H^+ \quad (5)$$

and results in per-titanic acid which can be detected by ultraviolet-visible (UV-Vis) spectroscopy measuring the corresponding absorbance at 407 nm. A calibration curve is obtained with known amount of hydrogen peroxide in ethanol as shown in Fig. S15.

$$H_2O_2(mM) = 2.212 * (A + 0.039) \quad (6)$$

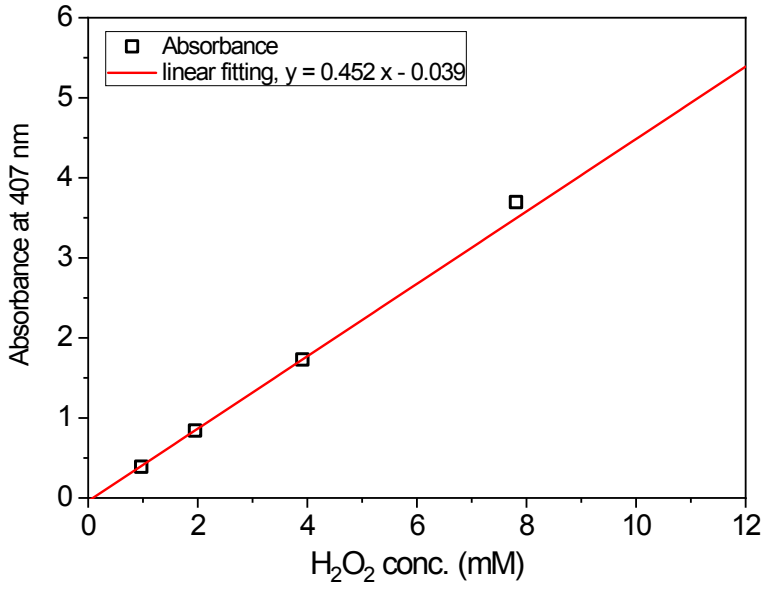

Fig. S17. Calibration graph for different concentration of H_2O_2 with titanium oxy-sulphate.

Fig. S16 shows absorbance spectra of plasma processed ethanol in presence of TOS scavenger from graphite anode and Fig. S17 reveals the absorbance spectra of TOS mixed plasma treated ethanol after subtracted from CuO QDs colloid absorbance obtained for various durations and currents respectively. The value of absorbance (A) is proportional to the amount of H_2O_2 present in the solution which can be calculated from the calibration curve and using equation 6.

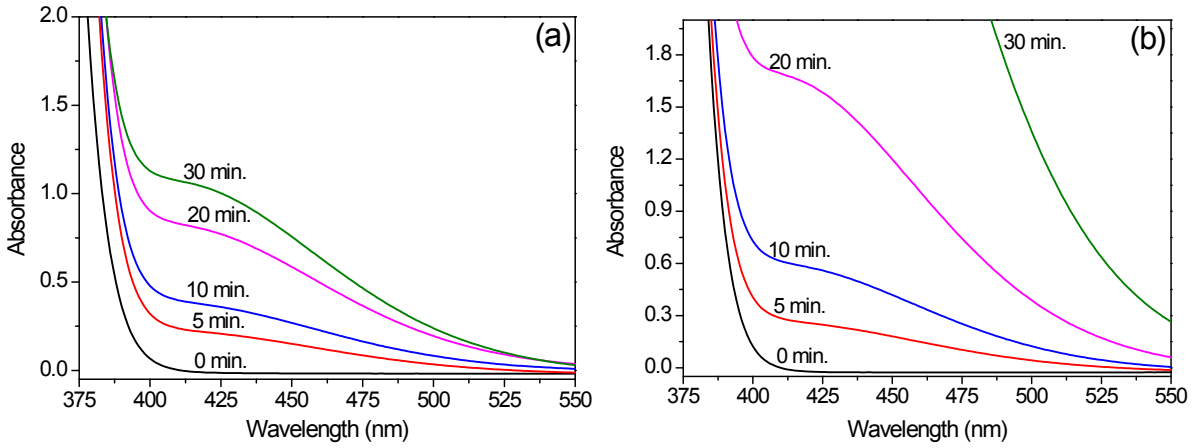

Fig. S18. UV-Vis spectral absorbance of plasma processed ethanol with graphite rod as anode at (a) 0.5 mA and (b) 3 mA mixed with titanium oxy sulphate scavenger for different intervals.

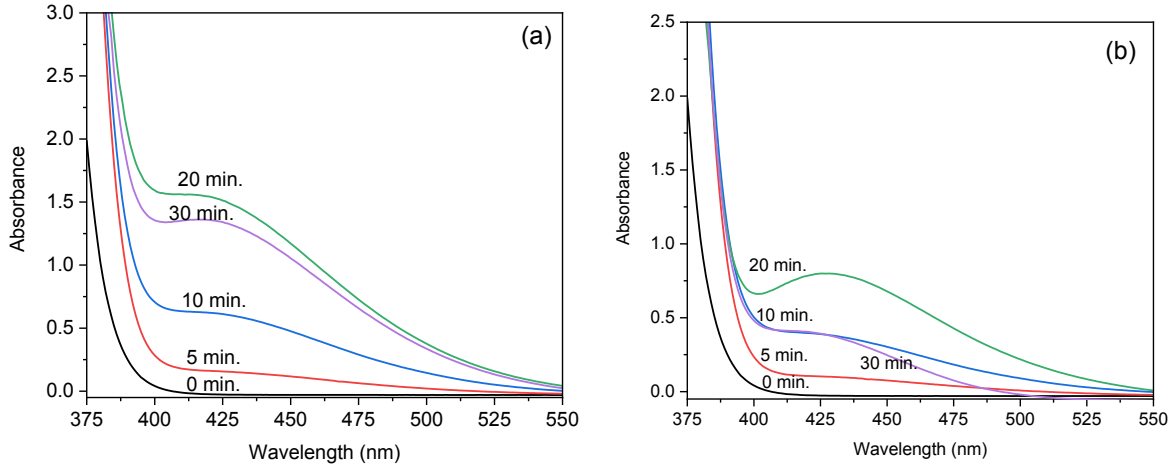

Fig. S19. UV-Vis spectral absorbance from plasma processed ethanol after deducted from CuO QD colloid absorbance both carried out from Cu foil as anode at (a) 0.5 mA and (b) 3 mA mixed with titanium oxy sulphate scavenger for different intervals.

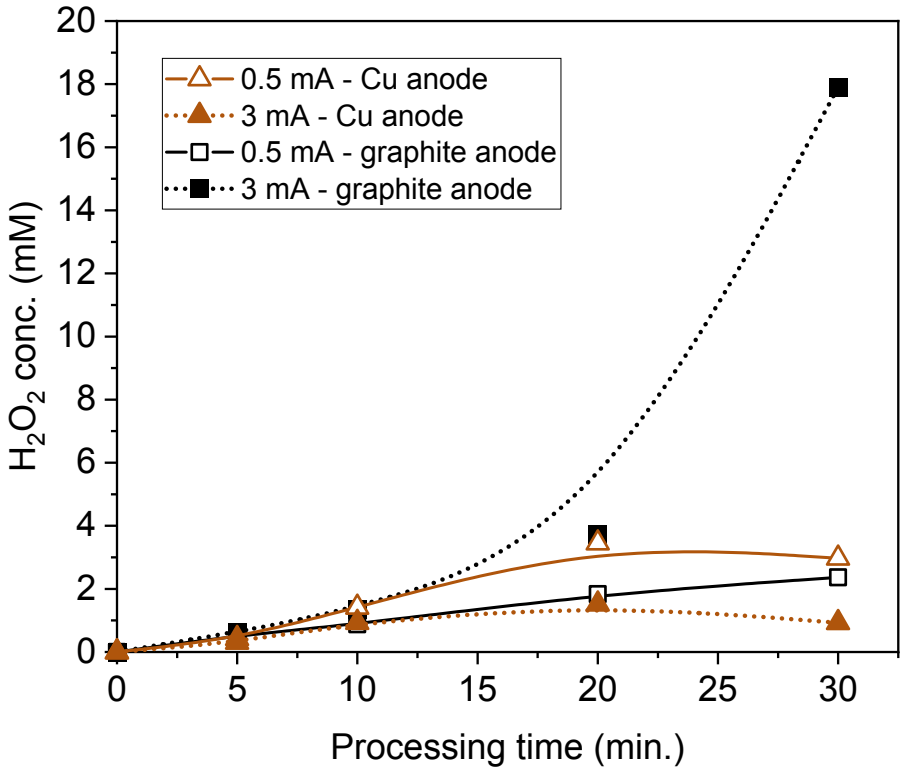

Fig. S20. Estimated hydrogen peroxide content in ethanol over different plasma process time, two different anodes.

10. pH

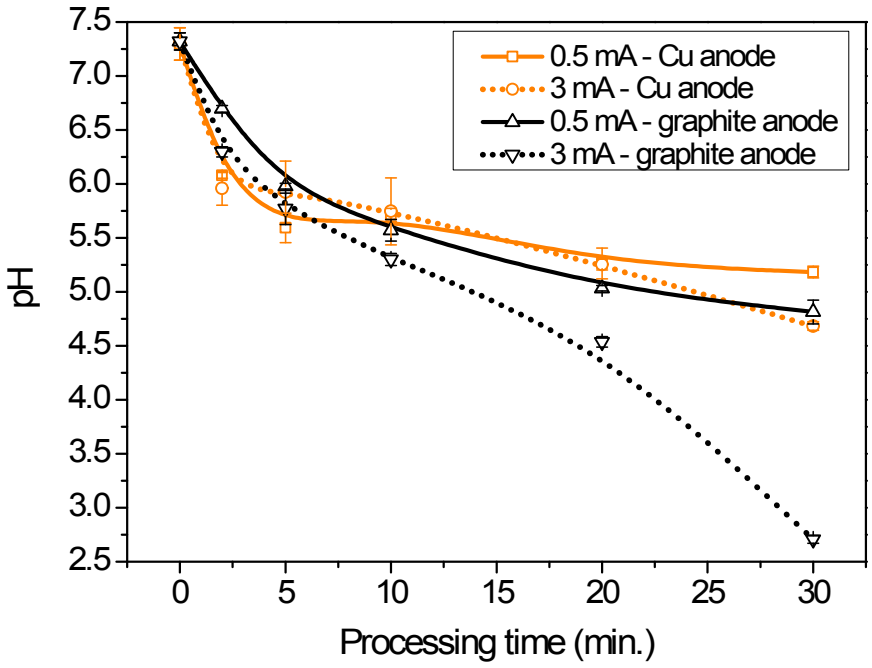

Fig. S21. Variation of pH over different plasma process intervals and two different anodes with errors bars related to three different measurement in the solution.

11. Estimation of H_2O concentration by Fourier Transform Infrared Spectroscopy (FTIR)

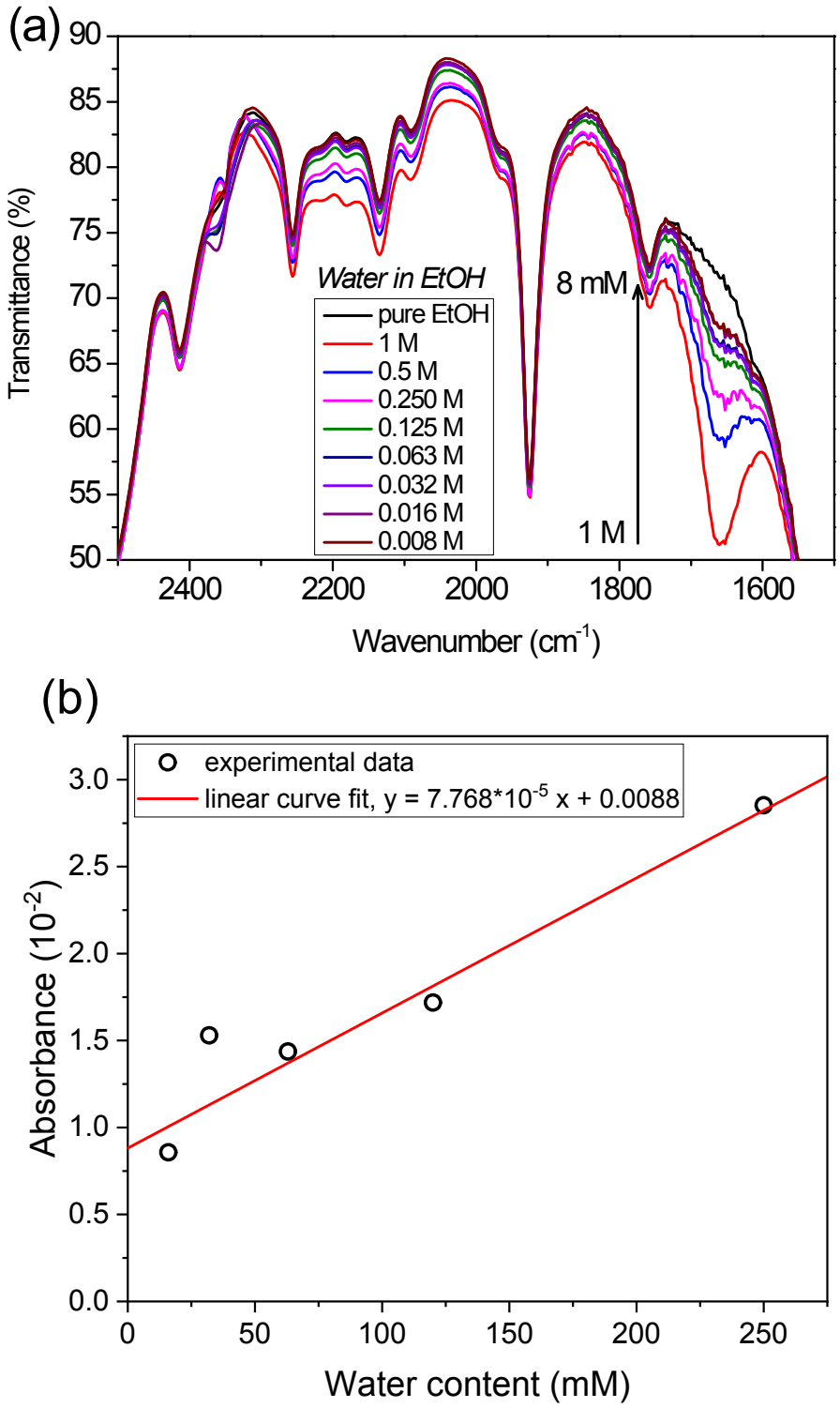

Fig. S22. Calibration plot for various concentration of H_2O in ethanol, (a) IR transmittance bands and (b) concentration graph.

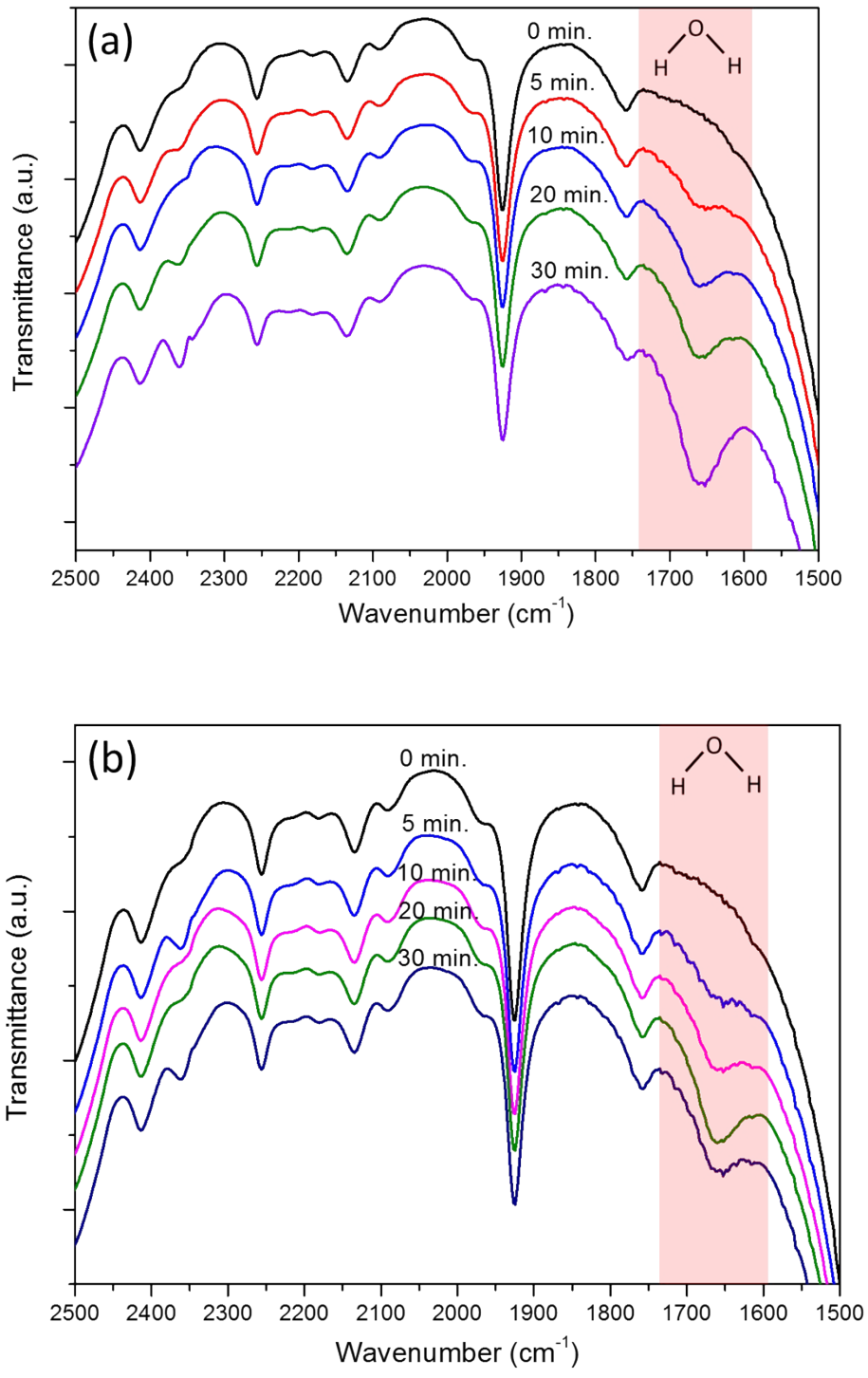

Fig. S23. IR transmittance bands of plasma processed ethanol with Cu foil, (a) 0.5 mA and (b) 3 mA for different process durations.

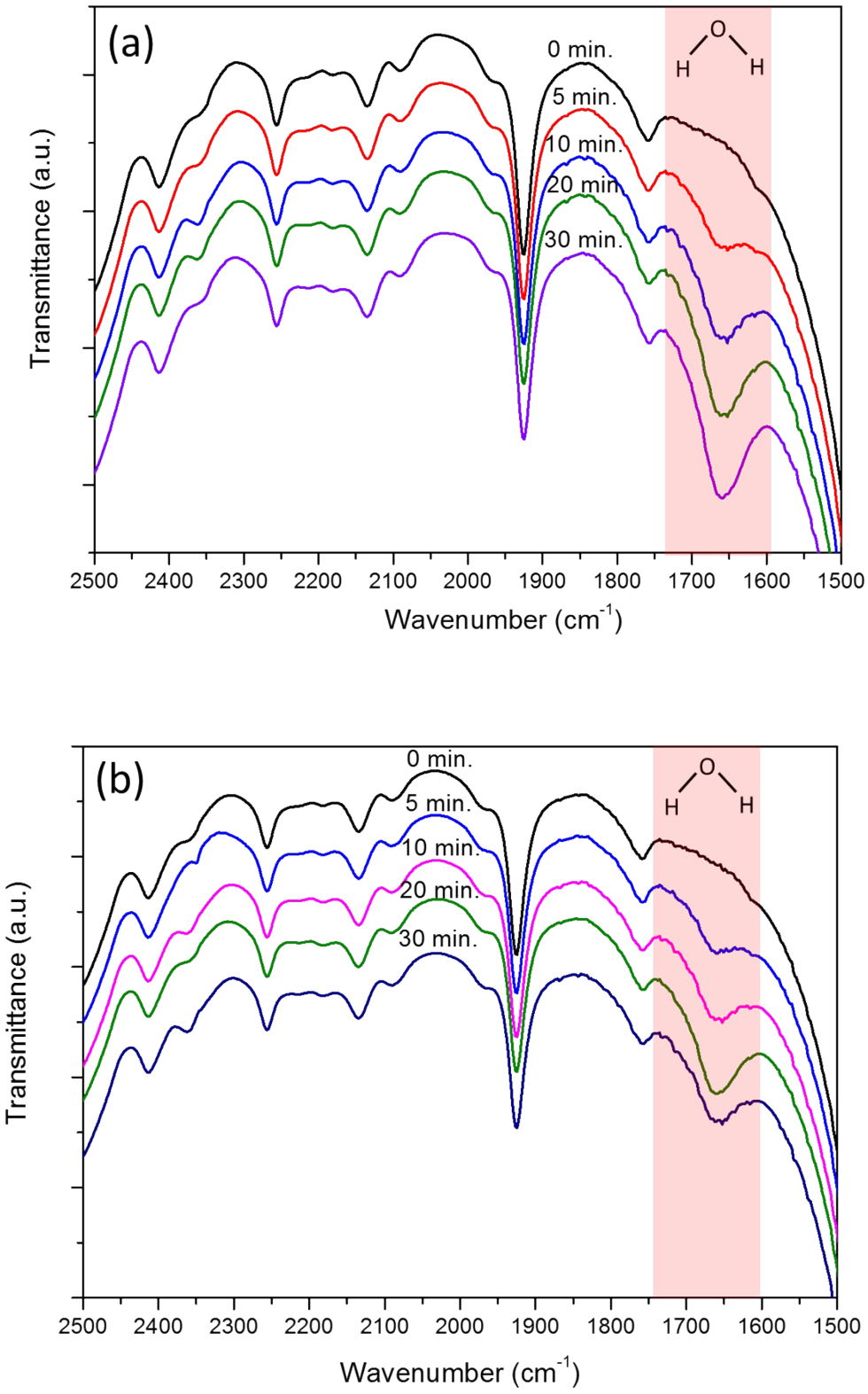

Fig. S24. IR transmittance bands of ethanol with graphite anode at (a) 0.5 mA and (b) 3 mA for different process durations.

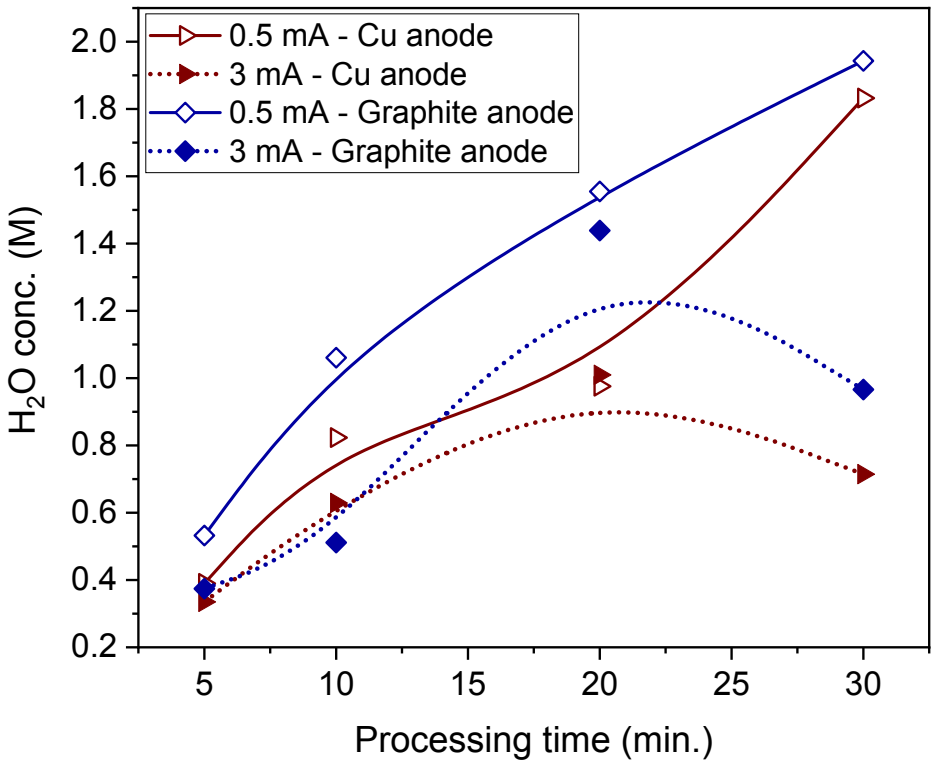

Fig. S25. Quantified water molecule content in plasma processed ethanol in comparison with two different currents.

12. Plasma optical emission spectroscopy and plasma-ethanol interface chemistry

Plasma optical emission spectroscopy (OES) can help identifying the different types of gas phase ions and radicals present in the plasma above the liquid. Fig. S25 shows the setup consists of a fibre optic tip is pointed towards the plasma above the liquid surface, inclined at a ~45^{o} angle with respect to the liquid surface and at a distance of ~7 mm from the microplasma.

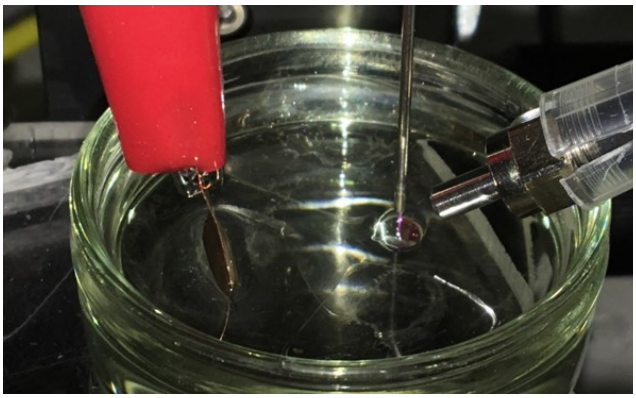

Fig. S26. OES measurement setup.

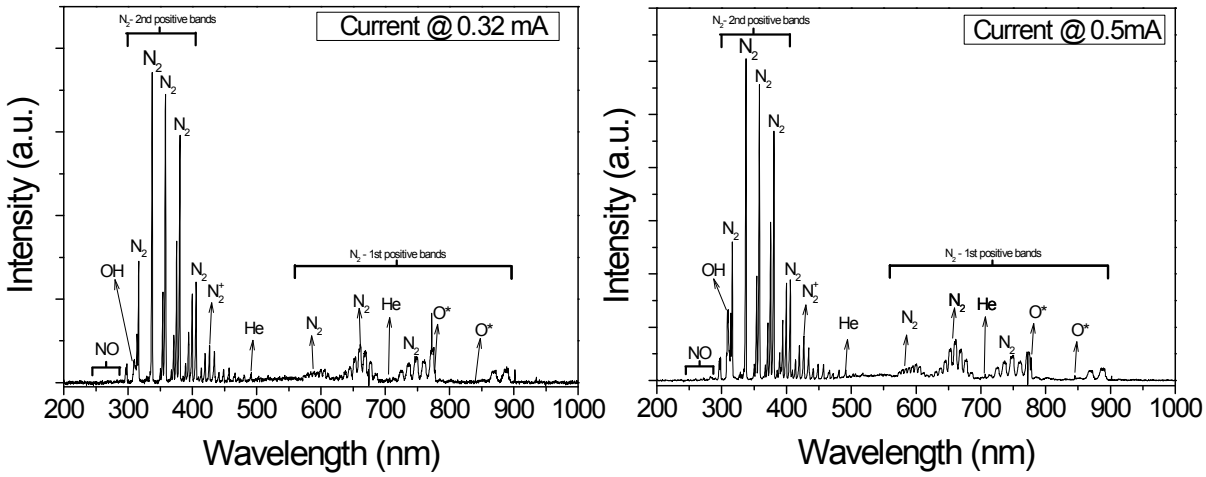

Fig. S27. OES spectra recorded from plasma above the liquid with Cu anode for various progressive currents for a set value 0.5 mA.

Fig. S25 shows the evolution of the emission spectra from the plasma with the current increasing to the set value of 0.5 mA. Similarly, Fig. S26 reports the spectra evolution of the plasma sustained with an increasing current up to the set-point of 3 mA. In both cases the Cu foil was used as anode. The emission lines in the spectra were identified through NIST[13] website and relevant literature and transition/reaction under consideration are summarized in table S3. In all cases, the spectra show weaker lines (447.8 nm, 491.7 nm and 706.3 nm) corresponding to He gas emitted from its excited states, He metastables (He*), undergoing relaxation. These He metastables (He^{*}) are produced through electron induced excitation as per equation 7.[14,15] Due to the interaction of the plasma with the surrounding atmosphere/ethanol and

possible turbulence at the interface, a range of emission lines from atmospheric gases such as nitrogen, oxygen, hydroxyl radicals etc. are observed and dominate all the spectra. Among all, the most intense emission lines arise from excited nitrogen that were identified as N_2 1st positive lines from 600 nm to 900 nm, N_2 2nd positive lines from 300 nm to 450 nm, minor lines from atomic oxygen (O^*) at 777.7 nm, 844.4 nm and OH band at 306 – 322 nm.[16,17] Further increase in the processing current leads to a general enhancement in the intensity of these atmospheric emission lines as well as to a more pronounced presence of atomic hydrogen lines, Balmer series H_α (656.5 nm) and H_β (486.2 nm).[14,18] Y. Lu *et al.*[19] reported similar series of emission lines in a DC driven capillary microplasma on water with Ar gas and in other works with He discharge in ambient air.[15,20] He metastable species (He*****) have sufficient energy to ionise atmospheric nitrogen and oxygen gas molecules by Penning ionisation[21,22] as per equations 8 and 9 respectively.[23] Liu *et al*.[24] has extensively discussed Penning ionisation of He metastables with water molecules in He/H_2O mixtures and other atmospheric gases with support of models. They concluded that the production rate of O, OH and H_2O_2 species depends on concentration of water molecules in the helium discharge. One of the most important paths leading to the production of O and OH species are from electron impact dissociation of ethanol from bulk liquid or possibly dissociation of water molecule from atmospheric humidity of reactions in equations 10 to 13. The interaction of helium metastables with water molecule can happen above the ethanol surface (equation 14 – 17) and can result in the production of HeH^+.[25] This species are important in the generation of H_3O^+ in the gas phase just above the liquid[26] (equation 18 and 19) and could be reabsorbed into ethanol or formed in the liquid as H_3O^+ leading to the increase in pH of the solution. However, the role of hydroxyl radicals (OH) can be important in our process as this would recombine (equation 20 and 21) close to the interface or in solution after absorption and lead to hydrogen peroxide in ethanol. Further increase in the anodic current contribute to increase hydrogen peroxide content (see Fig. 6d) and decrease the pH in the liquid (also see Fig. 6e) respectively.

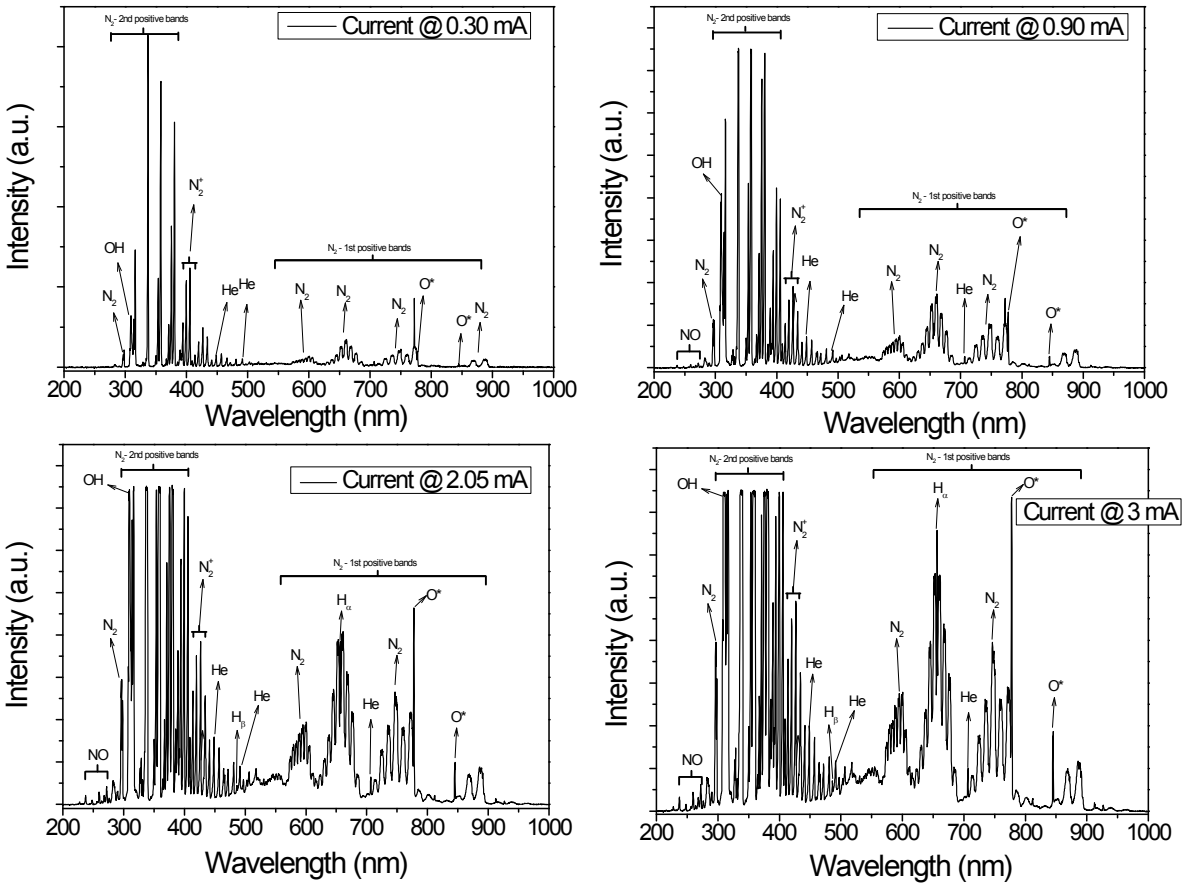

Fig. S28. OES spectra recorded from plasma above the liquid with Cu anode for various progressive currents for a set value 3 mA.

The excited N_2 and O_2 molecules lose energy via collision with other neutral molecules or other excited species and their excited energy is expended as gas heating near the interface that can induce more evaporation of ethanol from the surface.[27] The plasma locally heats up at the interface, volatile ethanol molecules could be subject to electron-induced ionisation into ethoxy and hydrogen radicals at the interface (equation 22). Nonetheless, we should note that there are no emission lines related to C_2 and CH radicals until 3 mA maximum processing current as seen in Fig. S26. Thus, various species such as OH, H^+, H_3O^+, H_2O_2 which are formed above the liquid or inside the liquid will diffuse into the bulk of the solution.

Table S4. Reaction scheme of gases in the microplasma assumed at the interface.

No.	Reactions
Electron induced ionisation and metastable generation in plasma:	
7	$e^- + He \rightarrow He^* + e^-$
Helium metastable induced reactions in plasma:	
8	$He^* + N_2 \rightarrow N_2^+ + He + e^-$

9	$He^* + O_2 \rightarrow He + O^* + O$
Electron impact dissociation in plasma by atmospheric humidity:	
10	$e^- + H_2O \rightarrow O^* + H_2 + e^-$
11	$e^- + H_2O \rightarrow H_2O^+ + 2e^-$
12	$2H_2O^+ \rightarrow H_3O^+ + OH$
Electron attached process in plasma by atmospheric humidity:	
13	$e^- + H_2O \rightarrow H^- + OH$
Helium metastable with water in plasma by atmospheric humidity:	
14	$He^* + H_2O \rightarrow H^+ + OH + He + e^-$
15	$He^* + H_2O \rightarrow OH^+ + H + He + e^-$
16	$He^* + H_2O \rightarrow H_2O^+ + He + e^-$
17	$He^* + H_2O \rightarrow OH + HeH^+ + e^-$
18	$HeH^+ + H_2O \rightarrow He + H_3O^+$
19	$H_2O^+ + H_2O \rightarrow OH + H_3O^+$
20	$OH + OH \rightarrow H_2O_2$
21	$OH + OH \rightarrow H_2O + O$
Gas or in liquid phase ethanol reaction:	
22	$CH_3CH_2OH + e^- \rightarrow CH_3CH_2O^- + H$

13. Thermogravimetric analysis

Thermogravimetric analysis (TGA) and differential scanning calorimetry (DSC) were performed to understand the sample purity from PiNE process. The measurements were carried out using Thermo fisher scientific - thermal analysis system, SDT Q600 V8.3 at heating ramp 5 °C/min from 20 °C to 1200 °C under nitrogen gas (N_2) flow of about 50 mL/min. Samples were initially prepared by drop casting the Cu-oxide colloid onto 90 μL SDT alumina cup at 70 °C for 30 min until the colloid dried inside the cup. Fig. S27 shows TGA/DSC curves of the QDs obtained for two different currents. All the samples show significant weight losses which were more prominent in the case of the sample at 3 mA and these losses were characterised with exothermic (positive peak) and endothermic (downward) peaks. An initial weight loss up to 200 °C is associated with removal of adsorbed water molecules[28] or any volatile such as residual ethanol solvent present in the samples. This observation can be corroborated from a report on TGA measurement with copper acetate monohydrates.[29] However, the 3 mA sample shows significant weight loss (~21 %) which is characterised by a small exothermic peak at 129 °C in the DSC plot of Fig. S27b. This can be due to the excess loss of unbonded or adsorbed hydrated molecules with copper species or on the surface of the QDs. Further weight losses above 200 °C were observed that can be identified at two different regimes, first around 240 °C (4.6 % for 0.5 mA and 37.5 % for 3 mA) related to the decomposition of loosely bonded solvent molecules with copper species as intermediate complexes that in the synthesis process converts completely to Cu-oxide.[30] Especially, the weight loss in the 3 mA sample around 226 °C (Fig. S27b) is characterised by a strong exothermic peak probably coming from crystallisation.[31] While between 300 °C and 700 °C, a pure CuO phase exists which later converts to Cu_2O probably due to reduction in the N_2 gas flow atmosphere.[31] Such a conversion of CuO to Cu_2O and finally to metallic Cu were reported in annealing experiments starting from CuO in vacuum[32] and in hydrogen atmospheres.[33] However, these reports also show that during these transformations, multiple phases were revealed to exist at a given temperature that depends on the size of the nanoparticles as well.[33] Also, at 949 °C (0.5 mA) and 1051 °C (3 mA), we observe a step in weight loss of about ~7 % accompanied with a large endothermic peak for the 3 mA sample (Fig. S28b). This is probably originating from loss of oxygen from Cu-oxide to Cu metal of the samples at those temperatures. Also, this clearly indicates a phase transition behaviour due to Cu-oxide reduction in N_2 atmosphere.[31] Beyond 1100 °C, the metallic Cu phase further undergoes a slight weight loss due to complete crystallisation as seen as endothermic peak. The observed shift and intensity of peaks in those temperatures between the (0.5 and 3 mA) samples with weight loss is probably from a difference in the mass. Thus, Cu-oxide obtained at 0.5 mA current shows an overall weight loss of 36.7 % whereas 3 mA reveals 67.1 %. In conclusion, this study corroborates our previous TEM results, i.e. that at higher current by-products are formed other than Cu-oxide.

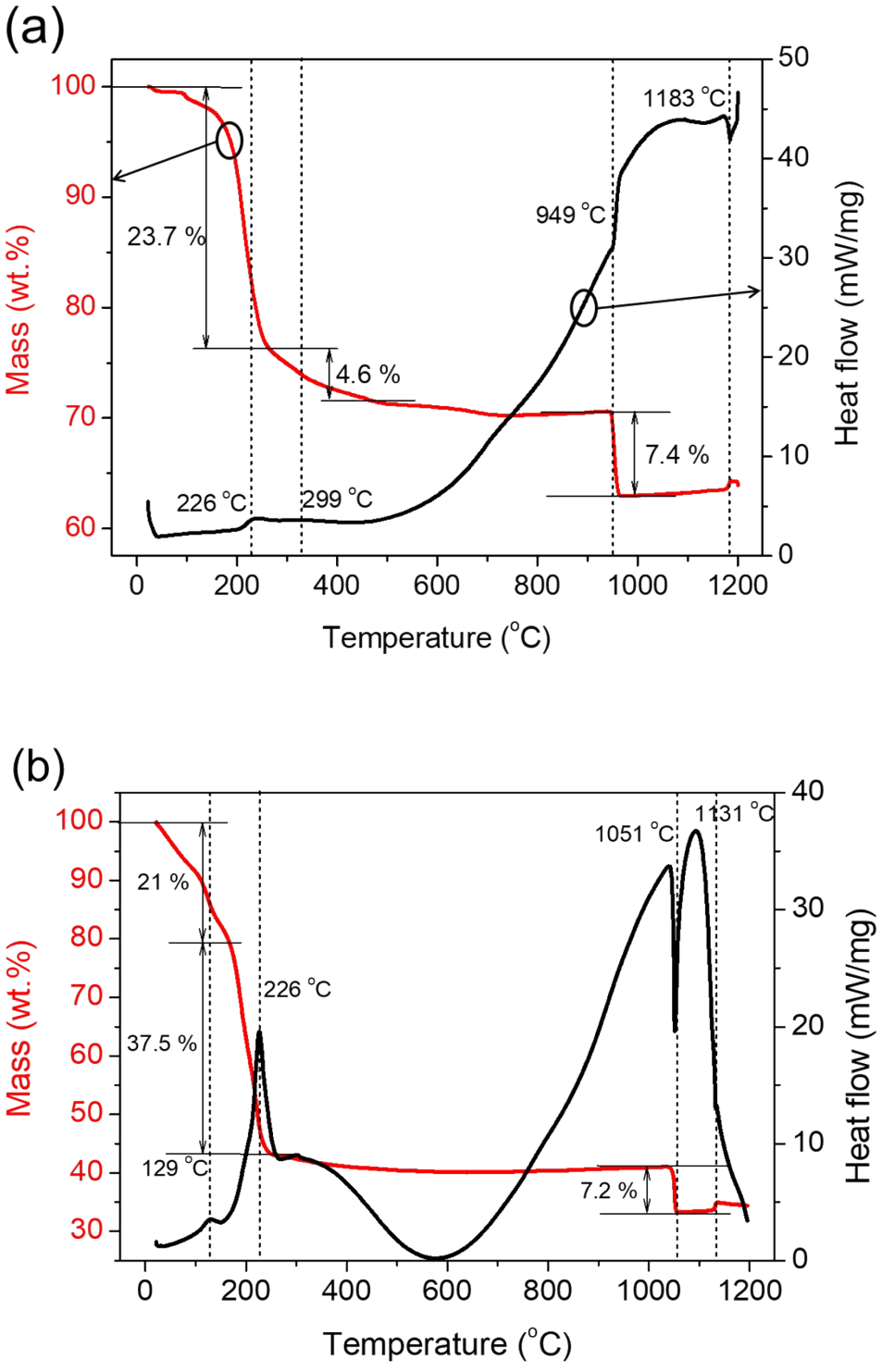

Fig. S29. TGA and DSC on Cu-oxide obtained from plasma process ethanol (a) 0.5 mA and (b) 3 mA, colloids dried in alumina crucible.

Reference

1 A. H. M. Al-Antaki, X. Luo, X. Duan, R. N. Lamb, W. D. Hutchison, W. Lawrance and C. L. Raston, *ACS Omega*, 2019, **4**, 13577–13584.
2 B. Balamurugan and B. R. Mehta, *Thin Solid Films*, 2001, **396**, 90–96.
3 M. U. Anu Prathap, B. Kaur and R. Srivastava, *J. Colloid Interface Sci.*, 2012, **370**, 144–154.
4 R. V. Kumar, Y. Diamant and A. Gedanken, *Chem. Mater.*, 2000, **12**, 2301–2305.
5 G. Qiu, S. Dharmarathna, Y. Zhang, N. Opembe, H. Huang and S. L. Suib, *J. Phys. Chem. C*, 2012, **116**, 468–477.
6 M. Vaseem, A. Umar, S. H. Kim and Y.-B. Hahn, *J. Phys. Chem. C*, 2008, **112**, 5729–5735.
7 D. I. Son, C. H. You and T. W. Kim, *Appl. Surf. Sci.*, 2009, **255**, 8794–8797.
8 M.-H. Chang, H.-S. Liu and C. Y. Tai, *Powder Technol.*, 2011, **207**, 378–386.
9 D. Han, H. Yang, C. Zhu and F. Wang, *Powder Technol.*, 2008, **185**, 286–290.
10 K. Borgohain, J. B. Singh, M. V Rama Rao, T. Shripathi and S. Mahamuni, *Phys. Rev. B*, 2000, **61**, 11093–11096.
11 D. Bhattacharyya, S. Chaudhuri and A. Pal, *Vacuum*, 1992, **43**, 313–316.
12 G. Eisenberg, *Ind. Eng. Chem. Anal. Ed.*, 1943, **15**, 327–328.
13 NIST: Atomic Spectra Database - Energy Levels Form, https://physics.nist.gov/PhysRefData/ASD/levels_form.html, (accessed 10 September 2018).
14 Q. Xiong, A. Y. Nikiforov, M. Á. González, C. Leys and X. P. Lu, *Plasma Sources Sci. Technol.*, 2012, **22**, 015011.
15 W.-C. Zhu, Q. Li, X.-M. Zhu and Y.-K. Pu, *J. Phys. D. Appl. Phys.*, 2009, **42**, 202002.
16 A. Sarani, A. Y. Nikiforov and C. Leys, *Phys. Plasmas*, 2010, **17**, 063504.
17 C. G. Parigger, G. Guan and J. O. Hornkohl, *Appl. Opt.*, 2003, **42**, 5986–5991.
18 D. Staack, B. Farouk, A. Gutsol and A. Fridman, *Plasma Sources Sci. Technol.*, 2008, **17**, 025013.
19 Y. Lu, S. F. Xu, X. X. Zhong, K. Ostrikov, U. Cvelbar and D. Mariotti, *EPL (Europhysics Lett.*, 2013, **102**, 15002.
20 N. Y. Babaeva and M. J. Kushner, *Plasma Sources Sci. Technol.*, 2014, **23**, 015007.
21 G. Nersisyan, T. Morrow and W. G. Graham, *Appl. Phys. Lett.*, 2004, **85**, 1487–1489.
22 K. L. Bell, A. Dalgarno and a E. Kingston, *J. Phys. B At. Mol. Phys.*, 1968, **1**, 303.
23 Q. Xiong, X. Lu, J. Liu, Y. Xian, Z. Xiong, F. Zou, C. Zou, W. Gong, J. Hu, K. Chen, X. Pei, Z. Jiang and Y. Pan, *J. Appl. Phys.*, 2009, **106**, 083302.
24 D. X. Liu, P. Bruggeman, F. Iza, M. Z. Rong and M. G. Kong, *Plasma Sources Sci. Technol.*, 2010, **19**, 025018.
25 T. SHIBATA, T. FUKUYAMA and K. KUCHITSU, *J. Mass Spectrom. Soc. Jpn.*, 1973, **21**, 217–221.
26 K. Sekimoto, R. Gonda and M. Takayama, *J. Phys. D. Appl. Phys.*, 2015, **48**, 305401.
27 A. Yanguas-Gil, J. L. Hueso, J. Cotrino, A. Caballero and A. R. González-Elipe, *Appl. Phys. Lett.*, 2004, **85**, 4004–4006.
28 Z. N. Kayani, M. Umer, S. Riaz and S. Naseem, *J. Electron. Mater.*, 2015, **44**, 3704–3709.
29 Z. Lin, D. Han and S. Li, *J. Therm. Anal. Calorim.*, 2012, **107**, 471–475.
30 M. S. Crespi, C. A. Ribeiro, V. C. M. Greenhalf and H. E. Zorel Jr., *Quim. Nova*, 1999, **22**, 41–46.
31 M. E. Brown, *Introduction to Thermal Analysis: Techniques and Applications*, Springer Netherlands, 2001.
32 S. Poulston, P. M. Parlett, P. Stone and M. Bowker, *Surf. Interface Anal.*, 1996, **24**, 811–820.
33 J. Y. Kim, J. A. Rodriguez, J. C. Hanson, A. I. Frenkel and P. L. Lee, *J. Am. Chem. Soc.*, 2003, **125**, 10684–10692.